

Structure and Ferroelectric Properties of Nanoimprinted Poly(vinylidene fluoride-*ran*-trifluoroethylene)

Hailu G. Kassa,[†] Ronggang Cai,[†] Alessio Marrani,[‡] Bernard Nysten,[†] Zhijun Hu,^{*,§} and Alain M. Jonas^{*,†}

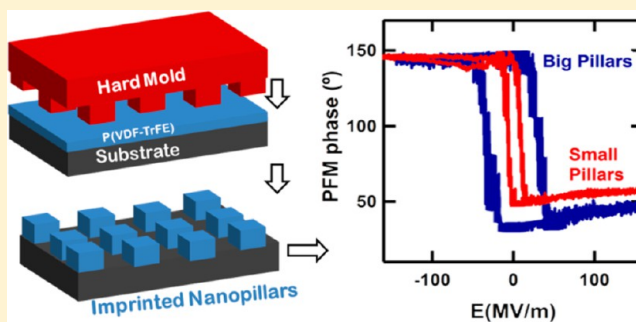
[†]Bio & Soft Matter, Institute of Condensed Matter and Nanosciences, Université catholique de Louvain, Croix du Sud 1/L7.04.02, B1348 Louvain-la-Neuve, Belgium

[‡]Research and Development Center, Solvay Specialty Polymers Italy S.P.A., Viale Lombardia, no. 20, Bollate (MI) 20021, Italy

[§]Center for Soft Condensed Matter Physics and Interdisciplinary Research, Soochow University, Suzhou 215006, China

S Supporting Information

ABSTRACT: Nanoimprint lithography (NIL) was used to shape thin films of a ferroelectric copolymer of vinylidene fluoride and trifluoroethylene (PVDF-TrFE), using a variety of molding shapes and imprinting conditions. The morphology of the layers was characterized by atomic force microscopy (AFM), and preferential orientation of the crystallographic axes was monitored by infrared microspectroscopy; in addition, the local ferroelectric properties were obtained by piezoresponse force microscopy (PFM). When the sample is imprinted in its paraelectric phase in conditions leading to complete confinement, in cavities of size lower than the natural lamellar length observed in a continuous thin film, the crystallographic *a* axis aligns preferentially parallel to the substrate, and the crystalline lamellae are of significantly reduced length. These characteristics translate in a strongly decreased coercive field and accelerated ferroelectric switching, which is in part ascribed to the improved coupling between the electric field and the properly oriented dipole moments. When decreasing the confinement either by leaving a residual film connecting the nanopillars, or by increasing the lateral size of the nanopillars above the natural lamellar length, or by using line molds where confinement only exists in one direction, or by using continuous films, the preferential orientation becomes less visible and the lamellar length increases, resulting in increased coercive and switching fields. Interestingly, the average length of the crystalline lamellae tends to correlate with the value of the coercive field. Finally, if the sample is imprinted in the melt, a flat-on setting of the crystalline lamellae ensues, with a vertical chain axis which is unfavorable for ferroelectric properties probed with a vertical electric field.



■ INTRODUCTION

Easy switching of polarization states of ferroelectric materials by an external electric field opens up the possibility to electrically control their properties and provides a physical basis for the fabrication of electronic devices like nonvolatile ferroelectric random access memories (FeRAM).^{1–5} Because of their high flexibility, low cost, and easy solution processability, organic ferroelectric polymers are getting considerable interest over inorganic ferroelectric materials.⁶ Poly(vinylidene fluoride) (PVDF) and its copolymers with trifluoroethylene (TrFE) are widely investigated ferroelectric polymers because of their large polarization and excellent switching characteristics, making them particularly attractive for nonvolatile memory applications.^{7–12} In order to integrate P(VDF–TrFE) in an all-organic low-power electronic device, it is desirable to decrease its switching voltage while preserving data retention. Since the switching voltage is related to the “coercive voltage” defined as the product of the coercive field by the film thickness, the coercive field being defined as the electric field required to zero the spontaneous polarization, lower switching voltages can be attained by decreasing the film thickness. This was however

reported to lead to deteriorated ferroelectric properties;¹³ recent reports indicate this to be related to preferential crystal orientation, a factor which can be controlled by proper processing.^{14–17}

Confining ferroelectric polymers into nanocavities was also reported to control crystal orientation, leading to improvements of the ferroelectric properties. Confinement of P(VDF–TrFE) can be achieved within the grooves of self-assembled organosilicate (OS) lamellar structures,¹⁸ by wetting nanoporous alumina templates to produce nanorods,^{19,20} or by using nanoimprint lithography (NIL).^{21–28} In these studies, the molecular orientation of P(VDF–TrFE) was affected by the confinement, resulting in modified ferroelectric properties. Among the aforementioned confinement techniques, nanoimprint lithography is especially promising because the fabricated regular nanopatterns can be used in applications like those of dense mass storage media.²⁸ Nanoimprint

Received: August 21, 2013

Revised: October 8, 2013

Published: October 23, 2013

lithography or nanoembossing is a low-cost and rapid technique which creates nanostructures by mechanically deforming a molten amorphous polymer film when pressed against a hard mold.²⁷

Recently, our group reported on the use of nanoimprint lithography technique to produce high-density regular arrays of P(VDF-TrFE) nanostructures where the orientation of the *c* (chain) and *a* axes was aligned in plane to the substrate.²⁸ The improved crystal orientation led to a significant decrease in the operational voltage by up to a factor of 5. Nevertheless, the detailed understanding of the influence of nanoimprint lithography on the crystallization process and the ferroelectric properties was not yet studied. Furthermore, no attempt was performed to tune the structure of the nanoimprinted P(VDF-TrFE) by playing with processing parameters or chain structure, although it is known that such parameters are critical on the crystal orientation and ferroelectric properties of P(PVDF-TrFE).^{4,29} Possible parameters to control are the composition of the PVDF copolymer and different external variables like temperature and pressure during imprint. Another important parameter is the residual film thickness, i.e., the thickness of the film that remains between the surface of the substrate and the protrusions of the mold, when the mold is fully pressed in the film. It was reported that this residual thickness has a critical role to play when crystallizing polymers in nanoconfinement.²⁵ Most importantly, the exact reasons for the dramatic improvement of the ferroelectric performances of P(VDF-TrFE) after nanoimprinting are not yet known. This knowledge will not only be of direct interest for plastic memory applications but will also provide basic information on the way the structure of semicrystalline polymers can be controlled by nanoconfinement under pressure and on the way nanoconfinement affects ferroelectricity.

In this paper, we report on the effect of confinement and processing parameters during nanoimprinting on morphology and crystal orientation as well as on the resulting ferroelectric properties of P(VDF-TrFE) nanostructures. As processing parameters, we essentially played with the initial film thickness and imprinting temperature. The geometrical constraints like size and shape (square or line) of the cavities of the hard mold used for the nanoimprinting process are also explored. The morphology and crystal orientation of continuous and nanostructured P(VDF-TrFE) are characterized by atomic force microscopy (AFM) and Fourier transform infrared spectroscopy (FTIR), respectively. The nanoscale ferroelectric properties are investigated by piezoresponse force microscopy (PFM). PFM hysteresis loops are used to get information about the coercive field while the PFM imaging mode is used to study more globally the switching of local polarization. Our results show the importance of the residual film thickness and lateral cavity size on the improvement of ferroelectric properties and illustrate the different crystal settings that result from using different imprinting conditions or molds.

■ EXPERIMENTAL SECTION

Sample Preparation and Methods. The poly(vinylidene fluoride-co-trifluoroethylene) copolymer (PVDF-TrFE) with 70/30 wt % of TrFE and $M_w = 230$ kg/mol was from Solvay Specialty Polymers (Italy) and used as-received. The melting temperature of this polymer was 143 °C, and its Curie transition temperature was 117 °C, as determined by differential scanning calorimetry at 10 °C/min. The P(VDF-TrFE) powder was dissolved in cyclohexanone (25 g/L). Thin films were prepared by spin-coating on a highly n-doped silicon substrate (resistivity 0.3–0.5 $\Omega\cdot\text{cm}$). The film thickness was varied by changing the spin speed. The resulting thin film thickness was

measured by profilometry and ellipsometry using 1.4 as the index of refraction. The SiO₂ hard molds were homemade by electron beam lithography (EBL). EBL is a standard lithography technique where a designed pattern is transferred from an electron-sensitive resist (PMMA) to the silicon substrate by lift-off and reactive ion etching procedures. Hard molds of different size and shape were prepared, with an effective patterned area of ca. (100 μm)². The limited patterned surface is the result of the slowness of EBL, preventing us to realize molds of larger patterning size. The height of the protrusions (i.e., the depth of the cavities) was controlled during the etching process. In order to separate the mold easily after imprinting, it was coated with a monolayer of perfluorodecyldimethylchlorosilane deposited from the liquid phase. The molds were silanized repeatedly after a few NIL experiments.

The nanostructures were fabricated by nanoimprint lithography using an Obducat 3-in. imprinter in a class 1,000 clean room environment. Initially, a continuous thin film of P(VDF-TrFE) was prepared by spin coating on the n-doped silicon substrate. Before applying pressure to imprint, the thin film was heated at T_{print} (usually, 125 °C). The print mold was pressed against the film under a pressure of 60 bar at T_{print} for 10 min to make sure that the nanocavities in the printing mold were completely filled. After the system was cooled to 60 °C, the pressure was reduced to zero and the mold was finally removed from the samples for characterization.

Characterization of the Morphology and Structure. The morphology of the continuous thin films and nanostructures was inspected using either a Multimode AFM (Nanoscope IV, Bruker) or an Agilent 5500 AFM (Agilent Technologies) in tapping mode using silicon cantilevers from Nanosensors (with a force constant of ~ 40 N/m and an apex radius of curvature < 7 nm). The molecular orientation of P(VDF-TrFE) samples was investigated by Fourier-transform infrared microscopy (continuum microscope from Thermo Scientific) in transmission mode thanks to the transparency of silicon in the useful range of the IR spectrum. To ensure a high signal-to-noise ratio, all spectra were averages of 128 scans with a resolution of 8 cm^{-1} . For line array samples, a polarizer was placed in the outgoing beam, with the polarization direction either parallel or perpendicular to the lines.

Quantitative Analysis of the Infrared Spectra. The infrared absorption spectra *A* were fit between 1030 and 1512 cm^{-1} by a model comprising a polynomial baseline (of order 3), the scaled signal of the bare silicon wafer, the scaled signal of amorphous P(VDF-TrFE) taken here as identical to the signal of molten PVDF reported in Figure 9 of Kobayashi et al.,³⁰ and the sum of seven crystalline peaks represented by Voigt functions of adjustable location, shape, width, and amplitude. The locations of the peaks were constrained to be within ± 2 cm^{-1} from the values reported by Prabu et al.³¹ for the crystalline peaks of P(VDF-TrFE) in this region (1430, 1404, 1342, 1292, 1184, 1127, and 1080 cm^{-1}). In order to decrease the number of fittable parameters, the width and shape of the weaker peaks at 1430, 1342, 1127, and 1080 cm^{-1} were held fixed to the average value found for the stronger peaks. The scale factors of the amorphous and silicon signals were two supplementary fittable parameters. However, the scaling factor of the Si signal was constrained to lie between 0.95 and 1.05, corresponding to the nominal variation of thickness of the Si wafers used in this study. A similar procedure was followed to fit the infrared signal between 650 and 1030 cm^{-1} ; in this case, however, only two crystalline peaks were used at 884 and 848.5 cm^{-1} , with the second peak having its width and shape held at the value of the stronger one; in addition, the baseline was a polynomial of order 5.

At the end of the fitting procedure, the scaled Si signal and the polynomial baseline were subtracted from the experimental signal, and the so-obtained absorption spectrum was normalized by division by the thickness of the P(VDF-TrFE) film expressed in nanometers. For imprinted samples, the thickness was taken as the one before imprinting, a valid approximation because the absorbance of the film is very small. The scaled spectrum of the fitted amorphous component was normalized similarly. The normalized spectrum of the crystalline component was obtained by subtracting the normalized amorphous component from the normalized baseline-corrected infrared spectrum.

The crystallinity was evaluated by taking the ratio of the areas of the normalized crystalline and global spectra between 1000 and 1500 cm^{-1} . The crystalline component was then divided by the crystallinity to obtain the pure crystalline spectrum; this spectrum, free of effects due to crystallinity, was used to evaluate the preferential orientation of the crystals.

Characterization of Ferroelectric Properties. An Agilent 5500 AFM (Agilent Technologies) system equipped with a Mac III Controller lock-in amplifier was adapted to the requirements of the piezoresponse force microscopy (PFM) technique. PFM was used to study the local polarization switching and local ferroelectric properties of continuous thin films and imprinted nanostructures. In order to make PFM measurements, the n-doped silicon substrate under the polymer film was used as a bottom electrode. A conducting boron-doped-diamond-coated Si cantilever (from Nanosensors) with a force constant of 0.02–0.77 N/m was used as a top electrode.

The PFM setup allows us to record local piezoresponse hysteresis loops (PHL's) of nanocells and continuous thin films, from which information about the coercive field is retrieved easily. The PHL's were obtained with the cantilever voltage modulated at the cantilever resonance frequency in order to enhance the signal-to-noise ratio (SNR) of the PFM amplitude and phase measurements. The polarization switching was inspected in PFM image mode using an oscillating voltage (amplitude 0.5 V) and dc bias simultaneously. All PFM measurements were done by applying an ac driving bias on the cantilever while applying the dc bias voltage on the sample substrate.

RESULTS AND DISCUSSION

Effect of Residual Layer on the Crystallization of Nanoimprinted P(VDF–TrFE) Nanostructures. Continuous P(VDF–TrFE) ultrathin films were spin-coated on a highly doped Si substrate. They were then annealed for 10 min at 125 $^{\circ}\text{C}$, a temperature above the Curie point (T_c) but below the melting point (T_m). Figure 1 shows AFM height and phase images of a 95 nm thick P(VDF–TrFE) continuous thin film consisting of randomly oriented lamellae.

In order to study the effect of the residual layer on the crystallization and its subsequent ferroelectric property, the ratio of the initial film thickness d to the cavity depth h of the mold should be known. For molds consisting of a square array of square cavities of period p and lateral cavity size l , the surface fraction of cavities is l^2/p^2 (ca. 0.5 in the present case). Then, a

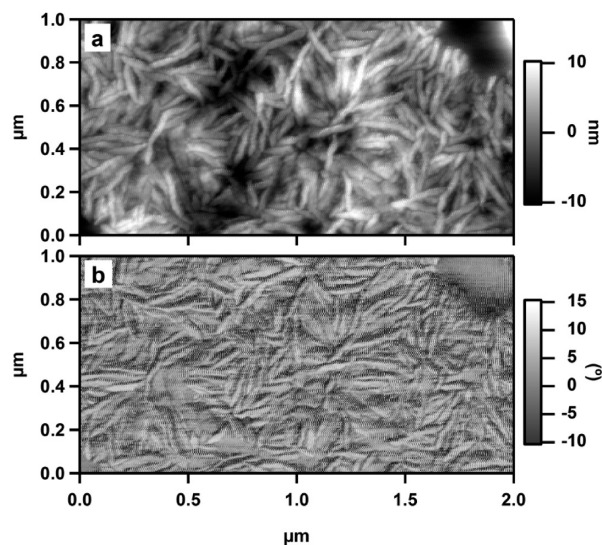


Figure 1. AFM morphology of a continuous ultrathin film. (a) Height and (b) phase images of 95 nm thick annealed continuous P(VDF–TrFE) thin film showing randomly oriented crystal lamellae.

residual layer exists after imprinting if $dp^2/l^2 \geq h$. In other words, when the film thickness d is much larger than the cavity depth h , there will be a residual layer between the nanopillars after embossing, a situation we call partial confinement. In the present work, imprinting with an initial film thickness (d) of 74 and 95 nm along with a hard mold of geometrical parameters $p = 350$ nm and $l = 250$ nm, resulted in 22 and 43 nm thick residual films, respectively. Imprinting was made at 125 $^{\circ}\text{C}$ for 10 min in the paraelectric phase of P(VDF–TrFE) copolymers. Of note, the imprinting temperature is the same as the annealing temperature of the continuous thin films.

Figure 2a–c shows typical AFM images of an imprinted sample with a 43 nm thick residual film. The full scale AFM height image (Figure 2a) shows only the topmost part of the regularly patterned nanosquares, which does not provide a clear view of the bottom residual layer between the nanosquares. To get a better view of the small crystalline lamellae over the whole scanned surface, we have combined together two separate images as shown in Figure 2b. This is achieved by having a height image that shows explicitly the topmost part of the nanosquares combined with another image that shows clearly the residual layer, each of the two images having its own color scale of identical range but different offset. Such composite topography images provide information that correlates very well with phase images (Figure 2c).

Imprinted samples under partial confinement display randomly oriented lamellae as shown in Figures 2b,c, both on the top of the nanoimprinted pillars and on the residual layer between them. The crystalline lamellae of partially confined nanostructures are structurally similar to those of continuous ultrathin films (Figures 1a,b). This is because the presence of a thin residual film led to a fast crystal growth below the protrusions of the mold, from which crystallization propagates into the square grooves of the mold. Thus, the final morphology is not solely controlled by the hard mold, but mainly by the residual film during the imprinting process.²⁵

On the other hand, if the topmost part of the hard mold is in contact with the Si substrate, there will not be any remaining polymer between the imprinted features. This leads to imprinting in conditions of complete confinement, where each nanopillar is totally isolated from the others with little or no underlying residual film. Full confinement is achieved when $dp^2/l^2 \leq h$. Using the same square mold used in the partial confinement experiments and a 50 nm initial film thickness of P(VDF–TrFE), 100 nm high nanopillars are obtained. Here, the 50 nm initial film thickness compared with the higher depth of the nanocavities (100 nm) ensures a direct contact between the hard mold and the substrate during imprinting. Figure 2d–f shows typical AFM images of fully confined arrays of nanopillars. The combined AFM height (Figure 2e) and phase images (Figure 2f) show the presence of only a few and discontinuous polymer filaments connecting individual pillars. Hence, the three-dimensional full confinement and an almost complete isolation of the nanosquares prevent the crystal growth propagating across the nanostructures. Nevertheless, the nanopillars remain polycrystalline.

To be precise on our morphology analysis, the length and distribution of 50 individual crystalline lamellae on each of the AFM images of Figures 1 and 2 have been measured manually. The distribution of the lamellae length of these samples is plotted in Figure 3. The annealed continuous ultrathin film sample has a wider distribution of lamellae length, and the average length of its lamellae is 207 nm by number and 217 nm

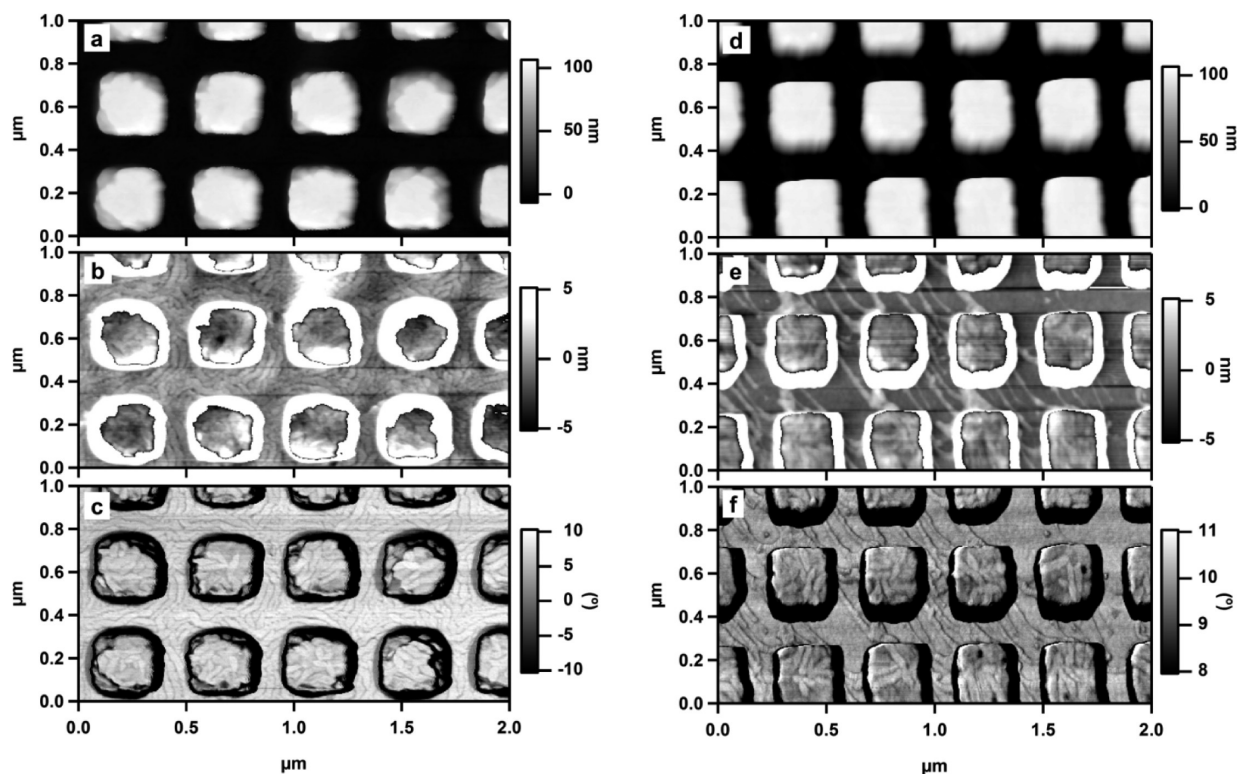


Figure 2. AFM morphology of an array of $(250 \text{ nm})^2$ imprinted P(VDF-TrFE) nanopillars. (a–c) AFM images of nanoimprinted structures in the partial confinement regime with 43 nm residual layer thickness: Height image (a), a combined height image of the topmost and bottom part of the nanoimprinted structures in the partial confinement regime showing the presence of crystal lamellae on the residual layer (b) and phase image (c). (d–f) AFM images of nanoimprinted patterns in full confinement regime: Height image (d), a combined height image of the topmost and bottom part of the array with almost no polymer left between the nanopillars (e) and phase image (f).

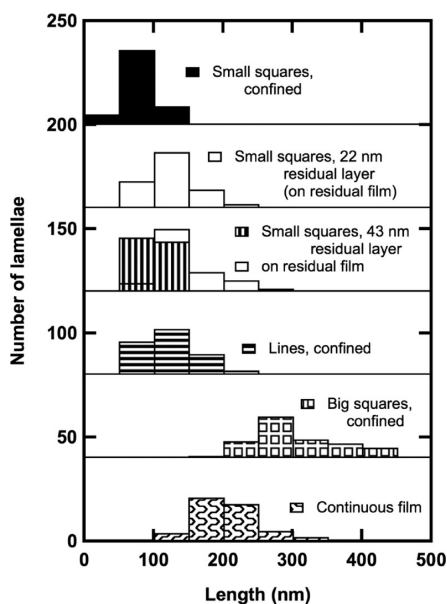


Figure 3. Length distributions of 50 individual lamellae taken from fully confined pillars of 250 nm lateral side (solid), imprinted pillars of 250 nm lateral side with 22 nm thick residual layer (white, on the residual film between them), imprinted pillars of 250 nm lateral side with 43 nm thick residual layer (vertical lines: on the nanopillars only; white: on the residual film between them), fully confined imprinted lines (horizontal lines), fully confined pillars of 500 nm lateral side (open squares), and continuous ultrathin films (folded patterns).

by surface. In contrast, nanopillars of 250 nm lateral side imprinted in conditions of full confinement have a narrower distribution of lamellar length with an average of 75 nm by number (82 nm by surface), well below the side length of the confining cavities.

Partially confined nanopillars with 43 nm residual thickness have a slightly larger average lamellar length by number of 96 nm (101 nm by surface), when measured over the nanopillars, whereas the average length on the residual film between the nanopillars is 145 nm by number (159 nm by surface). When the residual layer thickness decreases to 22 nm, the average lengths on the residual film drop to 123 and 131 nm for the number and surface averages, respectively (the average lengths could not be determined on the pillars). As a result, the average lamellar length falls in between the one of the continuous thin film and of the fully confined nanopillars. These observations already indicate a perturbation of the crystallization process by the (partial) confinement. The smaller lamellar length obtained when confining the crystallization process indicates a higher nucleation density compared to the continuous thin film. Similarly to other systems,^{25,27,32–36} this is most probably due to the division of the melt into many small cavities, which results in the exclusion of heterogeneous nucleation sites from many cavities and therefore a trend toward homogeneous nucleation occurring at lower temperatures.

Information on crystal orientation was investigated by Fourier-transform infrared spectromicroscopy (FTIR) in transmission. Grazing-angle X-ray scattering was not used because of the limited patterned area (ca. $(100 \mu\text{m})^2$), whereas electron diffraction was not selected owing to the difficulty to obtain

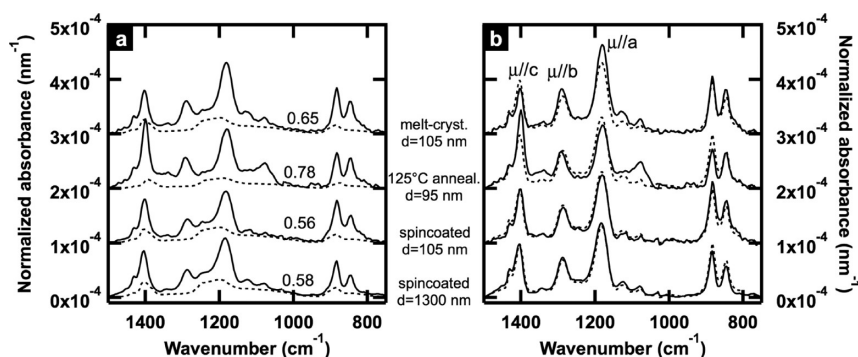


Figure 4. (a) Thickness-normalized infrared transmission spectra, corrected for baseline and Si absorption, of P(VDF–TrFE) continuous thin films. The dashed line is the amorphous component; the numbers are the crystallinity. (b) Corresponding thickness-normalized infrared spectra of the crystalline component, scaled to unit crystallinity. The dashed line is the spectrum of the reference spin-coated sample. From bottom to top: spin-coated film of 1300 nm thickness; spin-coated film of 105 nm thickness; film of 94 nm thickness, annealed at 125 °C; film of 105 nm thickness, crystallized from the melt. The curves are shifted vertically by integral multiples of 0.0001 nm^{−1} for clarity.

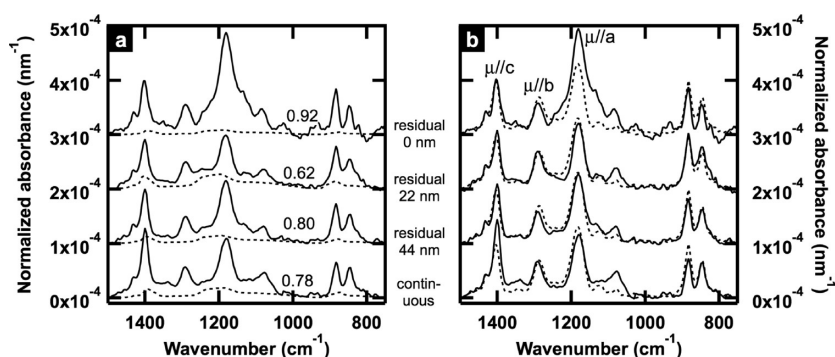


Figure 5. (a) Thickness-normalized infrared transmission spectra, corrected for baseline and Si absorption, of P(VDF–TrFE) thin films, imprinted with a mold of square cavities of 250 nm side and varying residual thickness as indicated. The dashed line is the amorphous component; the numbers are the crystallinity. (b) Corresponding thickness-normalized infrared spectra of the crystalline component, scaled to unit crystallinity. The dashed line is the spectrum of the reference spin-coated sample. The curves are shifted vertically by integral multiples of 0.0001 nm^{−1} for clarity.

quantitative information due to the extreme sensitivity of P(VDF–TrFE) crystals to electron radiation. Each sample provides its own characteristic FTIR spectrum resulting from the interaction of the incident electric field with the molecular vibration of the samples. In our experimental setup the electric field component of the IR beam is aligned parallel to the substrate within a finite opening angle due to the use of a Cassegrain condenser. Therefore, the absorption peaks correspond to vibrations having their transition dipole moments lying in this angular range, on average parallel to the substrate. The detailed molecular vibrations of the three crystal forms of PVDF, and their absorption band assignments can be found elsewhere.^{30,31} For the β phase, the strong absorption peak at 1400 cm^{−1} corresponds to the wagging vibration of CH₂ groups, which has a transition dipole moment μ_c parallel to the chain c axis, while the peak at 1180 cm^{−1} is attributed to an antisymmetric stretching and rocking vibration of CF₂ (μ_a parallel to the a axis). In addition, the absorption peak at 1288 cm^{−1} is assigned to the symmetric stretching vibration of CF₂ parallel to the polar b axis.²⁸

Figure 4a shows the thickness-normalized infrared spectra of a series of continuous films processed in different ways, together with the computed spectrum of their amorphous component (dashed line). From this decomposition (fully explained in the Experimental Section), the crystallinity of the samples could be obtained; it is also indicated in the figure. Because the amplitude of the crystalline absorption bands of

the samples is affected by both crystallinity and orientation, we have computed the spectra of the pure crystalline component, free from crystallinity-related effects, by computing the difference between the total and amorphous spectra, divided by crystallinity (Figure 4b). These pure crystalline spectra correspond to 100% crystallinity, and are thus only sensitive to orientation effects. One should be aware that, because Si has a relatively strong band at 1107 cm^{−1}, the P(VDF–TrFE) spectra cannot be reliably obtained between 1070 and 1140 cm^{−1}; however, this is a region where only small absorption bands are found for P(VDF–TrFE). In addition, the signal of the bare Si wafer is also quite rich and complex below 1000 cm^{−1}; therefore, the two P(VDF–TrFE) bands found in this region will not be discussed in the sequel, as they are likely to be much less accurate.

The two films measured after spin-coating (lower traces in Figure 4) exhibit a close crystallinity of about 57%, despite having rather different thicknesses (1300 and 105 nm, respectively). In addition, the spectra of their pure crystalline components almost superimpose (Figure 4b). Therefore, it is reasonable to assume that these films have relatively isotropic distributions of crystal orientation, in agreement with previous studies;³⁷ a reference crystalline spectrum was thus computed by averaging these two spectra. It appears as the dashed line in Figure 4b and will serve as reference for discussing relative orientations in the sequel. The film annealed in the paraelectric state at 125 °C (third trace from bottom in Figure 4) has a

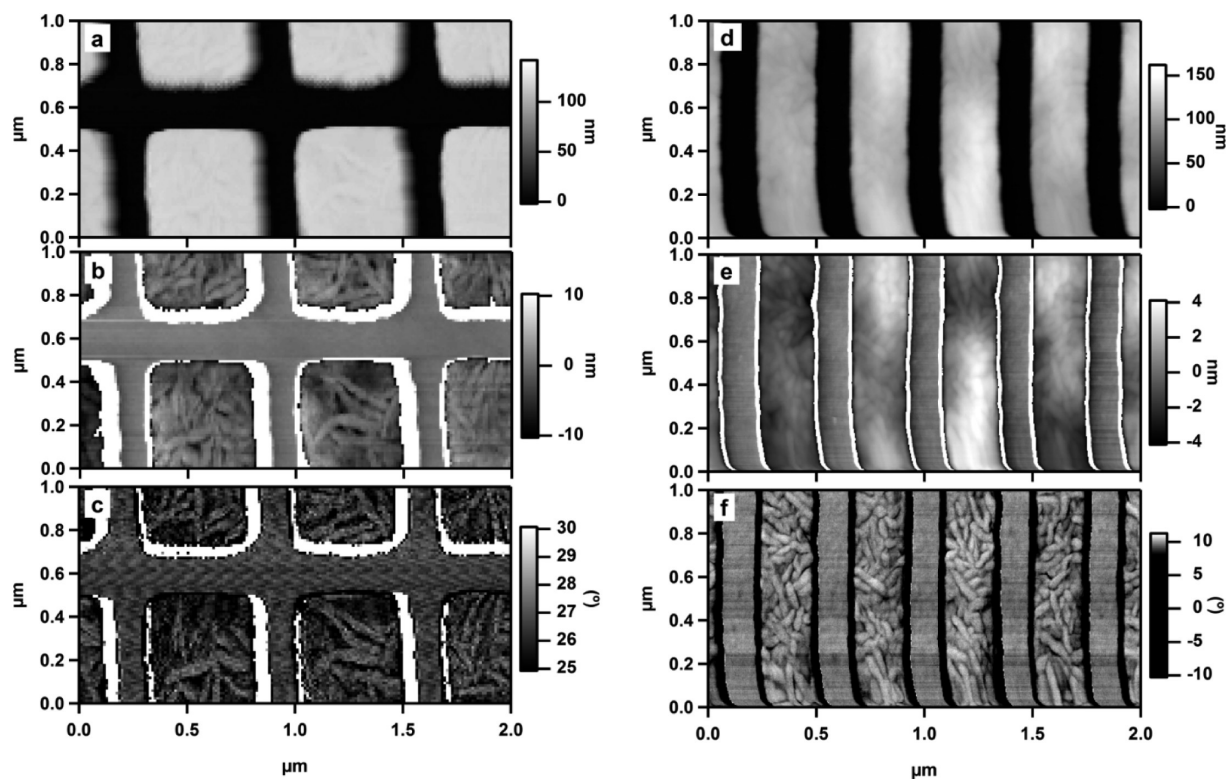


Figure 6. AFM morphology of imprinted P(VDF–TrFE) nanostructures of larger size. (a–c) AFM images of an array of fully confined nanoimprinted pillars of 500 nm side. (a) Height, (b) a combined height image of the topmost and bottom part of the nanoimprinted structures revealing long crystal lamellae on the topmost part, and (c) phase image. (d–f) AFM images of nanoimprinted lines in full confinement regime. (d) Height, (e) a combined height image of the topmost and the bottom part of nanopatterns containing shorter and wider lamellae on the topmost part, and (f) phase image, showing the lamellae more clearly.

significantly higher crystallinity, close to 80%. In addition, the pure spectrum of its crystalline component indicates that the chain c axis tends to align better in the plane of the substrate. In contrast, when crystallized from the melt, the a axis tends to lie in-plane, whereas the c axis slightly tilts toward the normal. This corresponds to a more flat-on orientation of the lamellae and is unfavorable for easy dipole rotation in the presence of a vertical electric field. These observations fully confirm previous reports on the effect of annealing temperature on crystal setting^{14,15,29,31,37} and therefore validate our methodology. However, it should be realized that the changes observed remain weak, which is due to the distribution of the orientation of the IR electric field resulting from the use of a Cassegrain condenser.

The infrared data for imprinted nanopillars of 250 nm lateral size, with various thickness of the residual layer, are displayed in Figure 5. Whereas the continuous thin film (lower trace in Figure 5) was characterized by a stronger absorption peak at $\sim 1400\text{ cm}^{-1}$ ($\mu_c||c$) compared to the reference isotropic sample, the imprinted film with no residual layer (upper trace in Figure 5) displays a strongly increased absorption peak at $\sim 1180\text{ cm}^{-1}$ ($\mu_a||a$), indicating a more in-plane (parallel to the substrate) orientation of the crystallographic a axis. This observation is consistent with our previous electron diffraction work,²⁸ which showed that samples imprinted in full confinement essentially displayed the (200) and (400) reflections, together with a weaker (001) reflection. Hence, it is likely that the imprinted sample corresponds to increased edge-on orientations of the lamellae (a and c in plane) compared to the reference spin-coated sample. In addition, the crystallinity of the fully

imprinted sample is increased by about 10% compared to the continuous film annealed at $125\text{ }^{\circ}\text{C}$.

In contrast, imprinted nanopillars with residual layers do not reveal any specific increase of peak intensity compared to the isotropic film, and their crystallinity is similar to or even lower than the one of the continuous film. This underlines the determinant role of full confinement in controlling crystal orientation and crystallinity during imprinting, and supports further our findings that showed the importance of nanoimprinting in controlling the local crystallization of polymers.^{25,28} One should however be aware that samples crystallized in conditions of partial confinement exhibit two very different regions, pillars and interpillar film, whose morphology was shown to be different by AFM; the infrared spectrum being the average of these two types of regions, caution should be exercised when discussing them.

Effect of Size and Shape on Crystallization of Nanoimprinted P(VDF–TrFE) Nanostructures. Once explored the influence of residual layer of imprinted nanostructures on the crystal quality and orientation, we turned our attention to systems that are fully confined in two dimensions (lines) and to imprinted pillars twice larger in lateral size (500 nm side). These samples will be compared with continuous thin films and fully confined pillars of 250 nm side. Hereafter, the $500 \times 500\text{ nm}^2$ imprinted square structures are referred to as “big pillars” to differentiate them from the previously discussed $250 \times 250\text{ nm}^2$ pillars which will be referred to as “small pillars”. The geometric parameters of the big square mold are the following: $p = 630\text{ nm}$, $l = 500\text{ nm}$, and $h = 140$

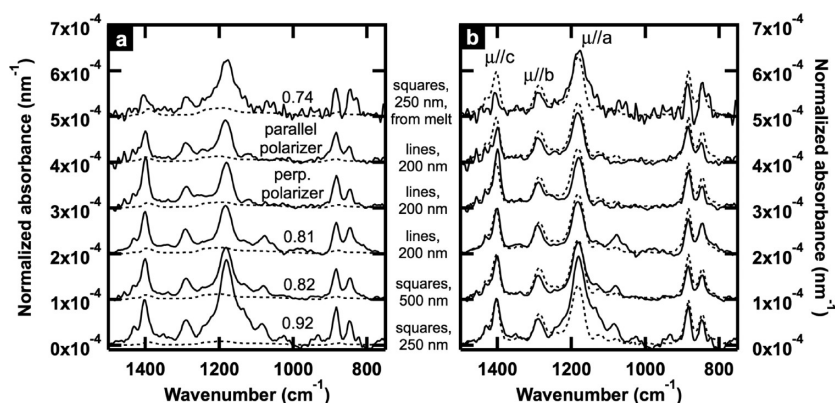


Figure 7. (a) Thickness-normalized infrared transmission spectra, corrected for baseline and Si absorption, of P(VDF-TrFE) thin films, with molds of cavities of varying size and shape, as indicated. All samples were imprinted in the paraelectric phase at 125 °C, except the topmost sample which was imprinted in the melt at 160 °C. The dashed line is the amorphous component; the numbers are the crystallinity. Two spectra of the line-imprinted samples were obtained with a polarizer placed in the beam, either parallel or perpendicular to the direction of the imprinted lines. (b) Corresponding thickness-normalized infrared spectra of the crystalline component, scaled to unit crystallinity. The dashed line is the spectrum of the reference spin-coated sample. The curves are shifted vertically by integral multiples of 0.0001 nm⁻¹ for clarity.

nm. With an initial film thickness of 95 nm, full confinement is thus achieved for big pillars.

Figures 6a–c show typical AFM images of imprinted big pillars. It is evident in both height and phase images of Figures 6a–c that there is no residual layer between the big pillars after embossing. This is a direct confirmation of a fully confined system. However, on the topmost part of the pillars, randomly oriented and longer crystalline lamellae are observed in Figures 6b,c.

The length distribution of the 50 crystalline lamellae is plotted in Figure 3. For imprinted big pillars the average length of the lamellae (298 nm by number; 312 nm by surface) is close to the one of the continuous thin film, and the length of the crystal lamellae is widely distributed from 180 to 400 nm. This is in contrast to imprinted small pillars for which the average length of the crystal lamellae (75 nm) was not only shorter than for bigger squares but showed also less variation of length. Obviously, here crystal nucleation is not severely affected by the splitting of the melt, which is logical since the lateral size of the cavities is well above the average lamellar length obtained in continuous films. Hence, regarding nucleation, the very notion of confinement appears to be relative to the natural, unperturbed size of the crystalline lamellae.

Line molds of period 400 nm and line width 200 nm were also fabricated to make fully confined imprinted lines. Like the square cavities when the initial film thickness d is much smaller than the protrusion height h , fully confined line patterns could be transferred from the mold. AFM Figures 6d–f show that almost no polymer is left in the regions between the protrusions of the print mold and the substrate because the initial 95 nm film thickness was much smaller than the 200 nm height of the trenches. AFM height and phase images of Figures 6e,f show crystalline lamellae that grow mostly edge-on at the top of the line patterns. The average length of the lamellae of these samples is 127 nm by number (139 nm by surface), and the lengths are less distributed than for continuous thin films. Here, it is important to note that the average size of the lamellae of the line patterns falls between the one of fully confined small squares and the one of fully confined big squares or continuous thin films.

The crystallographic orientation of imprinted big pillars and lines was also studied by FTIR and compared with imprinted

small pillars and annealed continuous thin films (Figure 7). Neither imprinted lines nor big pillars show any significant difference in the intensities of the absorption peaks, compared to the reference spin-coated film; in addition, their crystallinity of ~80% is comparable to the one of the annealed continuous thin film. This implies that imprinting using big square cavities ((500 nm)²) and lines (2D confinement) does not result in increased preferential orientation of specific crystallographic axes with respect to the substrate. Actually, imprinting with large cavities can be essentially considered as shaping the film with little beneficial effect on orientation or nucleation. This underlines the vital role of lateral size and shape of the cavities on controlling the crystal orientation of the P(VDF-TrFE) during embossing process.

FTIR was used to investigate further whether the crystals show or not any preferential orientation in the direction of the imprinted lines as the AFM images (Figures 6e,f) seemed to suggest. For this, we have used polarized IR to fix the polarization direction of the electric field. The external polarizer was aligned either parallel or perpendicular to the long axis of the lines. The three upper traces in Figure 7 shows FTIR absorption peaks of imprinted lines with the IR beam polarized parallel to the direction of the line, perpendicular to the lines, and without polarizer. It is obvious that the FTIR absorption peak at ~1400 cm⁻¹ ($\mu_{c||c}$) is stronger when the polarizer is perpendicular to the lines, which means that the c (chain) axis tends to be perpendicular to the lines. As expected, the IR absorption peaks of imprinted lines without polarizer have intensities between those polarized in the two directions. Since the c axis is perpendicular to the basal faces of the crystal, the lamellae should thus on average be more oriented in the direction of the lines. This preferential orientation is due to the influence of topographically patterned amorphous surfaces guiding the crystal growth in a specific direction, a phenomenon called graphoepitaxy.³⁸ In our specific case, the presence of rough silicon line grooves helped to guide the crystalline lamellae in the direction of the grooves. However, this effect is far from being perfect, as can easily be realized from the AFM pictures of Figure 6, which is not surprising considering the relatively short length of the lamellae compared to the width of the grooves. Accordingly, the dichroic ratio measured from the IR data, $(A_1 - A_2)/(A_1 + A_2)$ where A_1 and

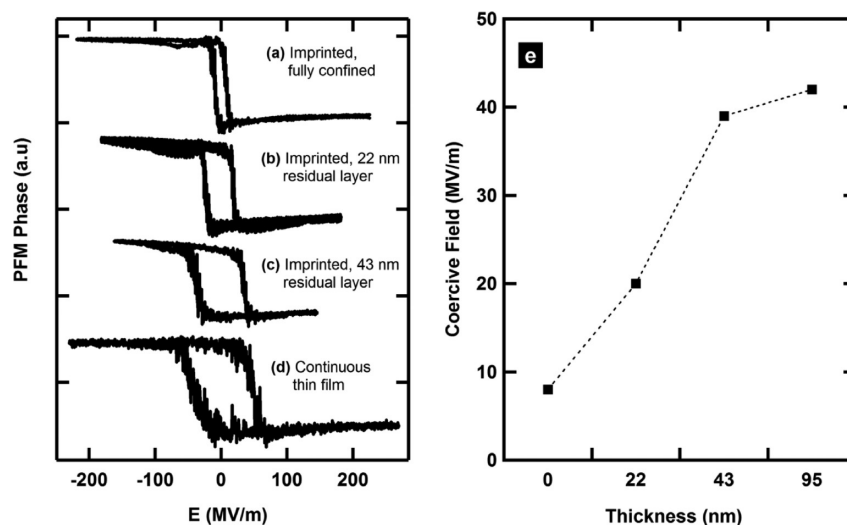


Figure 8. PFM-phase piezoresponse hysteresis loops (PHLs) of (a) an array of fully confined nanopillars of 250 nm side, (b) of a similarly imprinted array but with a 22 nm thick residual layer, (c) idem but with 43 nm thick residual layer, (d) of a continuous ultrathin film, and (e) the coercive field of the aforementioned samples as a function of the thickness of the residual layer or the thickness of the continuous thin film (95 nm). The loops were shifted laterally to center them on zero, due to slight experimental shifts resulting from built-in voltage or charging effects.

A_2 are the peak absorbances at $\sim 1400\text{ cm}^{-1}$ in the presence of the perpendicular and parallel polarizer, respectively, is only ca. 0.25, while it should be 0 and 1 for perfectly random and perfectly oriented samples, respectively.

Effect of Imprinting Temperature. Thermal annealing of P(VDF-TrFE) films is essential to control the molecular structure as well as the chain orientation,³⁷ as was shown above. Hence, the imprinting temperature should be crucial as well in determining the final microstructure and electrical performance of the nanostructures. We thus performed FTIR in transmission mode on samples that were imprinted in full confinement either above the melting temperature or in the paraelectric phase. Fully confined nanopillars of 250 nm lateral dimension imprinted at 125 and 160 °C for 10 min are compared in Figure 7. Interestingly, the nanoimprinting process exacerbates the trends seen on the continuous thin films. The film imprinted from the melt has a very low absorption peak at 1400 cm^{-1} ($\mu_c||c$), indicating that the chain axis is now almost fully perpendicular to the substrate; hence, the trend seen on the continuous films is amplified upon imprinting, leading to a much better alignment of the crystallographic c axis corresponding to flat-on crystals (a setting unfavorable for most applications). In addition, the slightly higher intensity at 1180 cm^{-1} ($\mu_a||a$) compared to the reference spin-coated film annealed at 125 °C implies that the crystallographic a axis also tends to orient itself parallel to the substrate. As for the sample imprinted at 125 °C, we already noted the preferential orientation of the a axis parallel to the substrate, whereas the c axis absorption remains strong, which corresponds to an edge-on setting of the crystalline lamellae. These FTIR studies thus underline the importance of controlling the thermal treatment during nanoimprint lithography as it results in entirely different crystalline orientations and therefore, as will be shown shortly, ferroelectric properties.

Nanoscale Ferroelectric Properties. Piezoresponse force microscopy (PFM) was then used to investigate the impact of the nanoprocessing parameters on the ferroelectric properties of the samples. The coercive field (E_c) of the nanostructured P(VDF-TrFE) can easily be accessed from PFM phase piezoresponse hysteresis loops (PHLs).^{39,40} Figures 8a–d

show PFM-phase PHLs of imprinted nanopillars and continuous thin films as a function of applied electric field.

For imprinted samples, we made sure that the conductive AFM tip was centered on top of the pillars. It should be noted that a series of PHLs were first taken while sweeping the voltage to increasing values; it was found that maximal voltages of $\pm 20\text{ V}$ were high enough to switch all the dipole moments of all the samples during a sweep (saturation). Interestingly, the coercive field of imprinted pillars of 250 nm side with 43 nm thick residual layer ($\sim 39\text{ MV m}^{-1}$) is almost the same as the one of the annealed 95 nm thick continuous thin films ($\sim 42\text{ MV m}^{-1}$). However, 100 nm thick fully confined pillars of 250 nm side have the lowest coercive field ($\sim 8\text{ MV m}^{-1}$) of all the samples, which is smaller than the E_c of continuous thin films by up to a factor of 5. The E_c of an imprinted sample with 22 nm thick residual layer is between the imprinted sample with 43 nm thick residual layer and the one of fully confined nanopillars. The E_c of all the different samples as a function of the thickness of the residual layer or sample thickness (for the continuous thin film) is plotted in Figure 8e. It is obvious from Figure 8e that the value of the coercive field increases when the thickness of the residual film increases, demonstrating clearly the importance of full confinement to make the switching of the dipole moments easier.

The ferroelectric properties of imprinted arrays of pillars with different lateral sizes and shape (lines) were also inspected by PFM phase PHLs (Figure 9). The coercive field of 130 nm thick imprinted pillars of 500 nm lateral side is $\sim 39\text{ MV m}^{-1}$, a value close to the E_c of continuous thin films ($\sim 42\text{ MV m}^{-1}$). Interestingly, the $\sim 20\text{ MV m}^{-1}$ coercive field of 200 nm thick confined line patterns is much lower than the one of a continuous thin film but still higher than three-dimensionally confined (250 nm)² pillars (Figure 9).

To complement the PHL results, the polarization switching behavior of the different samples was also studied by PFM imaging. In this mode, one measures the mechanical vibration of a conducting AFM tip in contact with the sample. An alternating electric potential of small amplitude is applied between the tip and bottom electrode, resulting in a periodic sample deformation due to the converse piezoelectric effect.

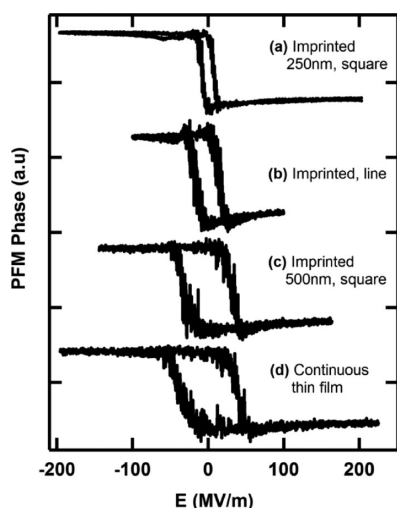


Figure 9. PFM-phase PHLs of (a) an array of fully confined nanopillars of 250 nm lateral side, (b) of an array of fully confined imprinted lines, (c) an array of fully confined nanopillars of 500 nm lateral side, and (d) of a 95 nm thick continuous thin film.

The amplitude and phase of the mechanical vibration are recorded by monitoring the motion of the tip, providing images which give information about the magnitude of the local polarization and its direction, respectively.³⁹ In order to observe the switching by PFM imaging, a $20 \times 20 \mu\text{m}^2$ square area was initially poled by applying a -30 V dc bias to the bottom electrode, resulting in a downward pointing dipole moment. Then, small squares of $4 \times 4 \mu\text{m}^2$ were poled by applying sequentially to the bottom electrode positive dc voltages from $+5$ to $+30 \text{ V}$ with an increment of 5 V . This resulted in partial upward flipping of the dipole moment. Finally, PFM images were recorded again on the $20 \times 20 \mu\text{m}^2$ square area at 0 V dc, revealing places where the dipole moment was flipped upward. Typical PFM amplitude and phase shift images of P(VDF-TrFE) imprinted nanostructures poled using the above conditions are shown in Figure 10. The clear color contrast between the negatively poled white background (polarization down) and the small dark squares poled by positive voltage (polarization up) is evident in the PFM phase image (Figure 10b) when the positive voltage is large enough. Qualitatively, when the reverse bias is $+5$ and $+10 \text{ V}$, the color contrast is very weak, indicating that the dipole moments are not fully switched (Figure 10b). However, when a positive reverse bias $\geq 15 \text{ V}$ is

applied, all the small squares are fully dark because all the dipoles are completely switched (180° rotation of the polar CF_2 unit).

To quantitatively compare our different samples, we define the “phase-contrast” $C = (A^+ \cos \phi^+ - A^- \cos \phi^-)$, with A the PFM amplitude and ϕ its phase, and where the superscripts $+$ and $-$ indicate that the values refer to an average performed over regions poled positively or negatively, respectively. The values of C , which are characteristic for the switching of the polarization, were interpolated and are plotted as a function of the switching electric field in Figures 11a,b.

Contrarily to the case of PHLs, this parameter is obtained from averages performed over regions containing many nanopillars. As shown in Figure 11a, the switching curve of an array of fully confined nanopillars of 250 nm side reaches its saturation plateau at a lower electric field than continuous thin films. Specifically, full confinement of the nanopillars decreases the half-reversal field from 110 MV m^{-1} for the continuous thin film to 55 MV m^{-1} . This is in agreement with the observation from PHLs that fully confined nanopillars have a lower coercive field. These lower switching and coercive field values enable easy writing and reading of information on ferroelectric memories.

The switching curves of partially confined nanopillars rest intermediate between fully confined and continuous thin film samples. However, one should be aware that the electric field is heterogeneous over the P(VDF-TrFE) sample because the thickness of the polymer varies from 22 or 43 nm (over the residual films) to 122 or 143 nm (over the nanopillars). As a result, the electric field which was calculated from the applied voltage using only the thickness of the nanodots is not an exact value over the whole sample and might actually be quite larger. Hence, the switching curves of these samples having residual layers should only be taken as qualitative.

The polarization switching of imprinted samples of different size and shape was also studied by PFM imaging. Figure 11b shows that imprinted pillars of $(500 \text{ nm})^2$ footprint have only a slightly higher half-reversal field (63 MV m^{-1}) than $(250 \text{ nm})^2$ imprinted squares (55 MV m^{-1}). The half-reversal field of imprinted lines is also significantly lower (54 MV m^{-1}). These results are thus not in complete agreement with the PFM phase PHLs, which we ascribe to the heterogeneity of the field over these complex nanostructures. This problem of heterogeneity does however not affect the PHLs, which were performed in

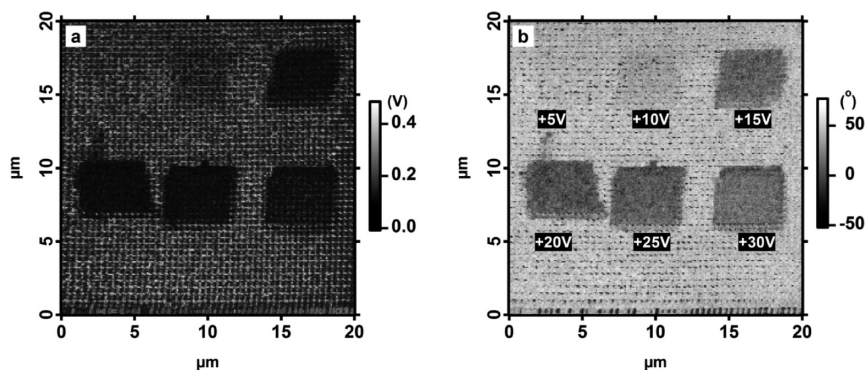


Figure 10. (a) PFM piezoresponse amplitude and (b) piezoresponse phase images of an array of nanopillars of 250 nm side, with 22 nm thick residual layers. In both images the background was polarized initially with a negative dc voltage of -30 V , and the smaller dark square areas were polarized with increasing positive dc voltages from $+5$ to $+30 \text{ V}$ as shown in (b). Both PFM images are recorded with a 0 V dc voltage.

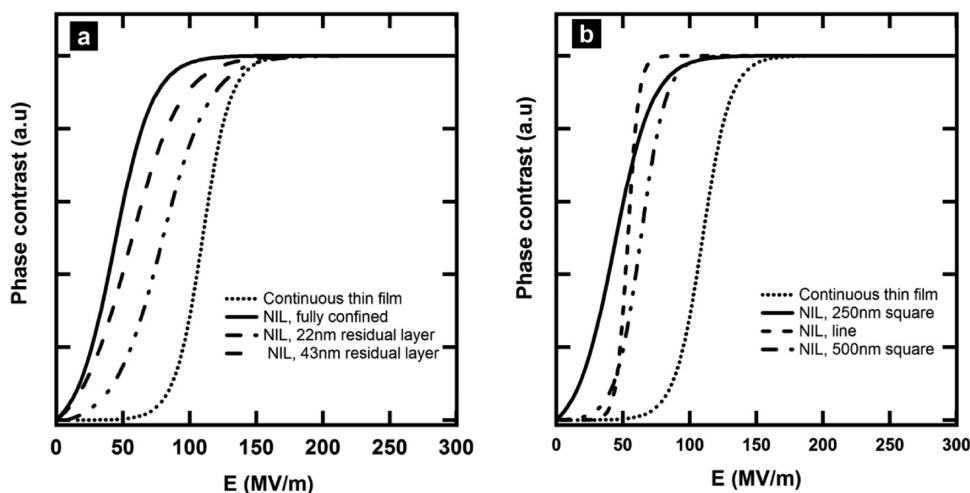


Figure 11. (a) PFM phase contrast vs the switching electric field (a) of annealed continuous ultrathin films (dotted line), of an array of fully confined nanopillars of 250 nm side (solid line), of an array of nanopillars of 250 nm side with 22 nm thick residual layer (broken dotted line), and with 43 nm thick residual layer (broken line). (b) PFM phase contrast vs the switching electric field of an annealed continuous thin film (dotted line), of an array of fully confined nanopillars of 250 nm side (solid line), of an array of fully confined nanopillars of 500 nm side (broken dotted line), and of imprinted lines (broken line).

the center of the nanopillars and will therefore be used for further discussion.

Correlation between Ferroelectric Properties and Structure. Previously, we had already shown that nanoimprinting could decrease the coercive field E_c of P(VDF-TrFE) significantly;²⁸ here we have investigated the effect of the remaining residual layer, cavity size and shape, and imprinting temperature, on the structure and electrical properties of the nanostructures. In this section, we attempt to correlate in more detail structure and coercive field. The coercive field reflects how easy the dipoles and ferroelectric domains can be switched, and it should thus depend on several structural factors, including, but not limited to crystal and dipole orientation, interchain distance, domain size, and interdomain interactions or coupling. It is thus unlikely that a single structural factor would be able to explain all our results.

A first factor to consider is the relative orientation of the dipole moments (aligned along the b axis) and of the axis of rotation of the dipole moments (the chain c axis) with respect to the vertically applied electric field. If the c axis is tilted by an angle θ away from the vertical electric field, while the b axis is rotated about c by an angle ϕ away from the plane containing the c axis and the electric field, the potential energy of the dipole in the field is $U_d = Em \sin \theta \cos \phi$, where E is the amplitude of the external electric field and m the one of the molecular dipole moment. If we accept that the rotation of the dipole moment about the chain axis requires to reach a threshold energy U_T , corresponding to energy barriers in the crystal, the coercive field, which measures the force required to start the dipole rotation process, is proportional to $U_T/(m \sin \theta \cos \phi)$. A sample with its a and c axes perfectly in the plane of the substrate would have $\phi = 0$ and $\theta = 90^\circ$, corresponding to the lower possible value of switching field. A sample with its c axis perfectly vertical would have $\theta = 0^\circ$ and a theoretically infinite coercive field. In agreement with this, the sample that was imprinted above the melting temperature, which precisely has a strongly vertical c axis, did not show hysteresis loops when probed by PFM (Supporting Information Figure S2). The sample imprinted in full confinement in the paraelectric phase at 125 °C has its a axis strongly in-plane, implying $\phi = 0$. This

again is in favor of lower coercive fields, the more so that the c axis itself will be more in-plane, in agreement with the observed low E_c . Within this very simple model, it becomes then easy to understand why partially confined nanopillars and continuous films have a higher E_c , which is due in part to the presence of more mixed polymer chain orientations, leading to an average weaker interaction between the applied electric field and the more randomly oriented crystals.

However, other factors also certainly play a role, as testified by the fact that samples having similar orientations as probed by FTIR do not have the same coercive field. This is for instance the case for the big pillars and the lines imprinted in full confinement and the smaller pillars imprinted in partial confinement. We note however that these samples, although being of similar crystallinity, objectively differ in the average length of their crystalline lamellae and that the general trend is for samples with shorter lamellae also to have lower coercive fields. It might thus be that the nucleation of ferroelectric domains is favored by the presence of crystal surfaces, acting as nucleation centers for dipole switching. This remains hypothetical, since the two observations might simply not directly depend on each other but depend instead on another, still hidden parameter. Nevertheless, this demonstrates clearly the need to decrease the lateral size of confined nanostructures for optimum structure and therefore ferroelectric properties.

CONCLUSIONS

We have demonstrated that by using nanoimprint lithography (NIL) a variety of nanostructured patterns can be transferred from a hard mold to ferroelectric P(VDF-TrFE) by imprinting in its paraelectric phase below the melting temperature. When the sample is imprinted in conditions leading to complete confinement, in cavities of size lower than the natural lamellar length observed in a continuous thin film, we observed a strong preferential orientation of the crystallographic a axis parallel to the Si substrate and lamellae of significantly reduced length. These changes resulted in a strongly decreased coercive field, and accelerated ferroelectric switching, which we ascribed in part to the improved coupling between the electric field and the properly oriented dipole moments. When decreasing the

confinement either by leaving a residual film connecting the nanopillars, or by increasing the lateral side of the nanopillars above the natural lamellar length, or by using line molds where confinement only exists in one direction, or by using continuous films, the preferential orientation becomes less visible and the lamellar length increase, resulting in increased coercive and (sometimes to a lesser extent) switching fields. Interestingly, it appears that the longer the crystalline lamellae, the higher the coercive field. In addition, we found that if the sample is imprinted in the melt, a flat-on setting of the crystalline lamellae ensues, with a strongly vertical chain axis which is unfavorable for ferroelectric properties probed with a vertical electric field. The same was found for a continuous thin film, but nanoimprinting was found to exacerbate this preferential orientation. These results reveal that nanoprocessing parameters like the degree of geometric confinement and imprinting temperature are crucial in controlling the crystal orientation and therefore ferroelectric properties. Our work should thus be of importance for the realization of low voltage, all organic flexible memories and devices.

■ ASSOCIATED CONTENT

■ Supporting Information

Figure S1: AFM composite topography image of nano-imprinted square pillars of 250 nm lateral side, separated by a residual film of 22 nm thickness; Figure S2: piezoresponse force microscopy (PFM) hysteresis loop of an array of fully confined nanopillars of 250 nm side and 100 nm height, imprinted above the melting point at 160 °C. This material is available free of charge via the Internet at <http://pubs.acs.org>.

■ AUTHOR INFORMATION

Corresponding Authors

*E-mail: alain.jonas@uclouvain.be (A.M.J.).

*E-mail: zhijun.hu@suda.edu.cn (Z.H.).

Notes

The authors declare no competing financial interest.

■ ACKNOWLEDGMENTS

Financial support was provided by the Fund for Research in Engineering and Agriculture (FRiA), the Belgian National Research Foundation (FNRS), the Louvain Foundation (Mécénat Solvay), and the Belgian Federal Science Policy (IAP P7/05). Z.H. acknowledges financial support from the National Natural Science Foundation of China (Nos. 91027040, 21074084) and the Natural Science Foundation of Jiangsu Province of China (No. BK2010213). The authors thank I. Huynen for discussions on electric field calculations by Comsol.

■ REFERENCES

- (1) Evans, P. R.; Zhu, X.; Baxter, P.; McMillen, M.; McPhillips, J.; Morrison, F. D.; Scott, J. F.; Pollard, R. J.; Bowman, R. M.; Gregg, J. M. *Nano Lett.* **2007**, *7*, 1134–1137.
- (2) Das, S.; Appenzeller, J. *Nano Lett.* **2011**, *11*, 4003–4007.
- (3) Scott, J. F. *Science* **2007**, *315*, 954–9.
- (4) Furukawa, T. *Phase Transitions* **1989**, *18*, 143–211.
- (5) Brondijk, J. J.; Asadi, K.; Blom, P. W. M.; de Leeuw, D. M. *J. Polym. Sci., Part B: Polym. Phys.* **2012**, *50*, 47–54.
- (6) Naber, R. C. G.; Tanase, C.; Blom, P. W. M.; Gelinck, G. H.; Marsman, A. W.; Touwslager, F. J.; Setayesh, S.; de Leeuw, D. M. *Nat. Mater.* **2005**, *4*, 243–248.
- (7) Heremans, P.; Gelinck, G. H.; Müller, R.; Baeg, K.-J.; Kim, D.-Y.; Noh, Y.-Y. *Chem. Mater.* **2010**, *23*, 341–358.
- (8) Naber, R. C. G.; Asadi, K.; Blom, P. W. M.; de Leeuw, D. M.; de Boer, B. *Adv. Mater.* **2010**, *22*, 933–945.
- (9) Youn Jung, P.; In-sung, B.; Seok, J. K.; Jiyoung, C.; Cheolmin, P. *IEEE Trans. Dielectr. Electr. Insul.* **2010**, *17*, 1135–1163.
- (10) Yang, Y.; Ouyang, J.; Ma, L.; Tseng, R. J. H.; Chu, C. W. *Adv. Funct. Mater.* **2006**, *16*, 1001–1014.
- (11) Lovinger, A. J. *Science* **1983**, *220*, 1115–1121.
- (12) Kepler, R. G.; Anderson, R. A. *Adv. Phys.* **1992**, *41*, 1–57.
- (13) Zhang, Q. M.; Xu, H.; Fang, F.; Cheng, Z.-Y.; Xia, F.; You, H. J. *Appl. Phys.* **2001**, *89*, 2613–2616.
- (14) Guo, D.; Stolichnov, I.; Setter, N. *J. Phys. Chem. B* **2011**, *115*, 13455–66.
- (15) Guo, D.; Setter, N. *Macromolecules* **2013**, *46*, 1883–1889.
- (16) Wu, Y.; Gu, Q.; Ding, G.; Tong, F.; Hu, Z.; Jonas, A. M. *ACS Macro Lett.* **2013**, *2*, 535–538.
- (17) Jung, H. J.; Chang, J.; Park, Y. J.; Kang, S. J.; Lotz, B.; Huh, J.; Park, C. *Macromolecules* **2009**, *42*, 4148–4154.
- (18) Kang, S. J.; Bae, I.; Shin, Y. J.; Park, Y. J.; Huh, J.; Park, S.-M.; Kim, H.-C.; Park, C. *Nano Lett.* **2010**, *11*, 138–144.
- (19) Lutkenhaus, J. L.; McEnnis, K.; Serghei, A.; Russell, T. P. *Macromolecules* **2010**, *43*, 3844–3850.
- (20) García-Gutiérrez, M.-C.; Linares, A.; Hernández, J. J.; Rueda, D. R.; Ezquerro, T. A.; Poza, P.; Davies, R. J. *Nano Lett.* **2010**, *10*, 1472–1476.
- (21) Hong, C.-C.; Huang, S.-Y.; Shieh, J.; Chen, S.-H. *Macromolecules* **2012**, *45*, 1580–1586.
- (22) Martínez-Tong, D. E.; Soccio, M.; García-Gutiérrez, M. C.; Nogales, A.; Rueda, D. R.; Alayo, N.; Pérez-Murano, F.; Ezquerro, T. A. *Appl. Phys. Lett.* **2013**, *102*, 191601.
- (23) Kang, S. J.; Park, Y. J.; Hwang, J. Y.; Jeong, H. J.; Lee, J. S.; Kim, K. J.; Kim, H. C.; Huh, J.; Park, C. *Adv. Mater.* **2007**, *19*, 581–586.
- (24) Zhang, L.; Ducharme, S.; Li, J. *Appl. Phys. Lett.* **2007**, *91*, 172906.
- (25) Hu, Z.; Baralia, G.; Bayot, V.; Gohy, J.-F.; Jonas, A. M. *Nano Lett.* **2005**, *5*, 1738–1743.
- (26) Hu, Z.; Muls, B.; Gence, L.; Serban, D. A.; Hofkens, J.; Melinte, S.; Nysten, B.; Demoustier-Champagne, S.; Jonas, A. M. *Nano Lett.* **2007**, *7*, 3639–3644.
- (27) Hu, Z.; Jonas, A. M. *Soft Matter* **2010**, *6*, 21.
- (28) Hu, Z.; Tian, M.; Nysten, B.; Jonas, A. M. *Nat. Mater.* **2009**, *8*, 62–7.
- (29) Matsushige, K.; Imada, S.; Takemura, T. *Polym. J.* **1981**, *13*, 493–499.
- (30) Kobayashi, M.; Tashiro, K.; Tadokoro, H. *Macromolecules* **1975**, *8*, 158–171.
- (31) Prabu, A. A.; Lee, J. S.; Kim, K. J.; Lee, H. S. *Vib. Spectrosc.* **2006**, *41*, 1–13.
- (32) Cormia, R. L.; Price, F. P.; Turnbull, D. *J. Chem. Phys.* **1962**, *37*, 1333–1340.
- (33) Montenegro, R.; Landfester, K. *Langmuir* **2003**, *19*, 5996–6003.
- (34) Taden, A.; Landfester, K. *Macromolecules* **2003**, *36*, 4037–4041.
- (35) Reiter, G.; Castelein, G.; Hoerner, P.; Riess, G.; Blumen, A.; Sommer, J.-U. *Phys. Rev. Lett.* **1999**, *83*, 3844–3847.
- (36) Massa, M. V.; Dalnoki-Veress, K. *Phys. Rev. Lett.* **2004**, *92*, 255509.
- (37) Mao, D.; Quevedo-Lopez, M. A.; Stiegler, H.; Gnade, B. E.; Alshareef, H. N. *Org. Electron.* **2010**, *11*, 925–932.
- (38) Givargizov, E. I. *J. Cryst. Growth* **2008**, *310*, 1686–1690.
- (39) Kalinin, S. V.; Morozovska, A. N.; Chen, L. Q.; Rodriguez, B. J. *Rep. Prog. Phys.* **2010**, *73*, 056502.
- (40) Soergel, E. J. *Phys. D: Appl. Phys.* **2011**, *44*, 464003.